OBSERVATION OF A STORMY WAVE FIELD WITH X-BAND RADAR AND ITS LINEAR ASPECTS

doi: 10.1142/S0578563407001587

OBSERVATION OF A STORMY WAVE FIELD WITH X-BAND RADAR AND ITS LINEAR ASPECTS

G. M. Jahid Hasan[1*] and Satoshi Takewaka[2]

Department of Engineering Mechanics and Energy

Graduate School of Systems and Information Engineering

University of Tsukuba, Tsukuba, Ibaraki, 305-8573, Japan

[1]*hasan@surface.kz.tsukuba.ac.jp*

[2]*takewaka@kz.tsukuba.ac.jp*

Fax: +81-029-853-5207

[*]*Corresponding author*

Abstract

An X-band nautical radar system was employed to observe the wave field generated during a storm around the research pier HORS in Hasaki, Japan. The radar system provides instantaneous distributions of wave crests in the near-shore region, with image sequences comprising a clear spatial and temporal variation of the wave pattern. The spectra of radar echo signals and water surface elevations from wave gauge records were compared, and a relatively high coherence for a particular bandwidth was observed. A sequence of radar images was filtered at the dominant frequency, which was used to estimate the wavenumber distribution of the refraction field. The Fast Fourier Transform (FFT) and Maximum Entropy Method (MEM) were used to estimate the wavenumbers. The estimated wave angles were then compared with linear refraction analyses. The water depths along the pier were also estimated using the linear dispersion relationship and compared with the surveyed depths. The linear estimates of hydrodynamic parameters during the passage of the storm are presented in this paper to demonstrate the potential of radar measurements in capturing essential characteristics of coastal dynamics.

Keywords: X-band radar; spectral analysis; refraction angle; depth inversion; storm event.

1. Introduction

The near-shore is the energetic region of the coastal environment where ocean waves shoal and interact with local morphology. As waves approach an open shoreline from deep water, they undergo large changes. Refraction, non-linearity and breaking affect wave properties. Changes in bathymetry can occur on time scales as short as hours due to presence of large storms. Data are especially difficult to collect during periods of large waves or strong currents. However, these conditions often represent the most energetic periods for hydrodynamics, morpho-dynamics and are the times of greatest scientific interest. X-band nautical radar is an imaging tool that is capable of tracking the movements of wave crests over large spatial regions and is becoming popular for coastal studies nowadays. The advantage in using an X-band radar system is its ability to monitor the coastal processes remotely and continuously, under calm conditions as well as stormy. This paper describes the linear aspects of a wave field observed with an X-band nautical radar during an energetic sea state.

Traditional in situ instruments can record precisely the variations of water surface elevations, velocities, sediment concentration, bottom elevation etc. These instruments are a powerful tool for monitoring near-shore regions. However, the measurements are expensive and limited in spatial extent. Further, during energetic sea states it is not easy to maintain data collection. Remote sensing techniques provide a feasible alternative because they allow sampling over large spatial extents (meters to kilometers) and temporal scales (seconds to

years).

Aerial photography is one of the earliest forms of remote sensing used to image wave fields, and nowadays video cameras or radars are becoming popular for continuous monitoring. Video cameras can monitor the sea surface patterns with high temporal resolution typically several images per second. However, the spatial coverage is limited with a single camera, which necessitates multiple cameras in order to gain wide coverage. Video cameras can provide color images, which enable to detect wave breaking, suspension of foams, sediment concentrations etc and to trace their temporal and spatial variations. Video cameras are usually mounted on a tower standing on the shore, providing slanted views, and rectified montages of video images from different cameras enable analyses of wave and current fields and morphological processes. One severe shortcoming is that the use of video cameras is limited to daylight hours and fair atmospheric conditions.

Estimation of hydrodynamic and mopho-dynamic parameters from video images is just one of a suite of recent techniques. Stockdon and Holman [2000] developed an advanced method to estimate near-shore bathymetry based on video image processing. They calculated wavenumber components from the gradient of the wave phase propagation of the dominant incidental band, and a linear dispersion relationship was used to estimate water depths. Piotrowski and Dugan [2002] used a sequence of video images of shoaling ocean waves to retrieve maps of water depth and currents. Some other studies also used inversion techniques

to retrieve bathymetry [e.g. Aarninkhof *et al*., 2005]. Video images have also been analyzed to understand coastal features such as wave run-up [Holland and Holman, 1999; Holland *et al*., 1995], detection and measurement of submerged sand bar systems [Lippmann and Holman, 1989; Enchevort and Ruessink, 2001; Ranasinghe *et al*., 2004], foreshore beach slopes [Plant and Holman, 1997] etc.

Some of the limitations of video imaging can be overcome using X-band radar. The pixel intensity of a radar image corresponds to the relative amount of backscatter signal from sea surface of the emitted radar beam, which allows its use during night and under slightly rainy and stormy conditions as well. Radar image sequences with high spatial resolution and large coverage (extending up to several kilometers) offer a unique opportunity to study individual waves and wave fields in space and time. The drawbacks of commercial marine radars are their relatively low sampling rate of around one image every 2.5 s and difficulties in detection of sediment suspensions and wave breaking states from the echo backscatter.

The use of X-band radars in coastal studies is becoming popular in these days. Young *et al*. [1985] first described an approach using a three-dimensional Fourier transform analysis on a sequence of radar images. The resulting wave number spectra were inverted to frequency spectra with information of the water depths. Izquierdo *et al*. [2005] compared the ocean wave field derived from X-band radar and wave-rider buoy measurements by spectral analysis. The comparison showed good agreement between variations of significant wave height, peak

frequency and mean period obtained from both devices. The estimated directional spectra from their radar observations were broad banded due to coexistence of storm generated swell and wind wave. Bell [1999, 2001] succeeded in determining near-shore bathymetry after analyzing X-band radar images. He applied a linear depth inversion technique, considering peak period from Fast Fourier Transforms (FFT), and wave celerity from cross correlations between sequences of images. Bell *et al*. [2004] used two different types of radar (X-band radar and MMW radar) to infer water depths and tried to improve further the depth inversion. Recently, Dankert and Rosenthal [2004] developed an empirical inversion method for determination of time series of ocean surface elevation, which maps from X-band nautical radar image sequences in a relatively deep region. For validation of their result, the wave elevation time series derived from the inverted radar data sets were compared with wave records, and acceptable accuracy was established. Takewaka and Nishimura [2005] analyzed radar images for run-up analyses during a storm. Takewaka [2005] also analyzed time averaged X-band radar images to quantify shoreline position and inter-tidal foreshore slopes, while Ruessink *et al*. [2002] analyzed images to locate near-shore bar crests.

This paper describes the general applicability of radar observations to energetic sea states, and in particular the analyses of radar backscatter echoes to confirm linear properties of a storm generated wave field. Radar images were captured at Hasaki Oceanographical Research Station (HORS) (Fig. 1) during a storm event. The frequency distribution and wave

number variations were estimated from power spectra in order to check the dominant frequency and its directional variation during wave propagation. Radar images were filtered at the dominant frequency, and corresponding refraction angles were estimated and compared with linear wave ray computations. The methodologies and accuracy of the results are discussed to demonstrate the potential of radar measurements.

Fig. 1

2. Set-up

2.1 *Research pier HORS*

X-band radar measurements were conducted at the research pier HORS of the Port and Airport Research Institute (PARI), located in Hasaki, Japan. The main facilities are a 400 m length pier extending into the Pacific Ocean and a research building located nearly 108 m backward from the mean shoreline position. HORS is on an almost straight sandy coast approximately 17 km long with Choshi Fishery Port at the south end and Kashima Port at the north end of the coast. The pier is located approximately 4 km from Kashima Port. Water surface elevations are measured with several wave gauges mounted on the pier, and the bottom profile along the pier is surveyed on weekdays.

2.2 *Radar system*

The radar system employed in this study is a conventional marine X-band radar, usually

installed on fishing or recreational boats. The radar antenna (approximately 2.8 m in length) is installed on the roof of the research building 17 m above the mean sea level as shown in Fig. 2. The figure has an aerial view of the HORS pier. The antenna rotates with a period of approximately 2.5 s and transmits with a beam width of 0.8° horizontally and 25.0° vertically. The echo signals from the sea surface, generally called sea clutter, are captured with a specially designed A/D board installed on a computer.

Fig. 2

2.3 *Radar echo image*

Measurements of the sea state using nautical radar are based on the backscatter of electromagnetic pulse from the sea surface. The echo signals from X-band radar was used to generate images with 1024 pixels in horizontal and 512 pixels in vertical. The horizontal extent of an image is 5556 m (3.0 nautical miles) and the vertical extent is 2778 m (1.5 nautical miles) and each pixel corresponds to a square of 5.4 m. The gray images have pixel intensities between 0 to 255 with brighter pixels corresponding to stronger backscatter.

Figure 3 shows a typical radar image captured during a stormy condition. The slanted white lines extending in the long-shore direction are oblique wave crests and vertical strip in the middle of the figure is the pier. The radar is located at the midpoint of the bottom edge of the diagram indicated by a black dot. Figure 3 also shows the coordinate system used in this study. The x-axis corresponds to the along-shore extent and positive towards Choshi Fishery

Port and the *y*-axis coinciding with the pier and oriented in the offshore direction.

Correlation between radar echo intensity variation and water surface elevation was examined by estimating coherence and phase of the signals which is described in Appendix.

Fig. 3

2.4 *Meteorological and sea state conditions*

The typhoon BANYAN (Typhoon #7, T7, 2005) traveled through the western edge of the Pacific Ocean from 21st to 31st of July 2005. The track of the typhoon is shown in Fig. 4. Radar echoes were collected continuously for several hours during the passage of the typhoon. Figure 5 shows the measured atmospheric pressure as well as the wind speed and direction during the passage of the typhoon at Choshi Fishery Port recorded by the Japanese Meteorological Agency (JMA). The typhoon was closest to HORS near 22 hr on July 26 when the lowest atmospheric pressure was recorded, and the radar images of this hour were used here for analyses.

Fig. 4 and 5

The offshore waves were measured by the Nationwide Ocean Wave Information Network for Ports and Harbors (NOWPHAS) station at Kashima Port where the mean water depth is approximately 24 m. Tide levels were measured by JMA at Choshi Fishery Port. The variations of tide level, significant wave height $H_{1/3}$, significant wave period $T_{1/3}$ and significant wave direction $\theta_{1/3}$ are shown in Fig. 6. The significant wave height increased up to 3.69 m due to the passage of the typhoon, whereas the significant wave period and wave

direction remained almost constant. Table 1 shows the wave records for the analyzing period.

Fig. 6 and Table 1

2.5 *Bathymetry*

The water depth data used in this study were collected from different survey records around HORS. Table 2 summarizes the period and coverage of the surveys. The water depth data from a bathymetric chart (map no. 6367-7) were compared with other surveyed depths along the pier (x = 0 m) as shown in Fig. 7. The comparison implies an almost unchanged region beginning at $y \approx 700$ m and the active sediment zone can be considered up to approximately 6 m water depth.

Fig. 7 and Table 2

3. Wave Field: Overall State

3.1 *Linear estimation of shoaling and refraction*

Wave height variation when the centre of the typhoon BANYAN was closest to the pier was estimated using linear theory. The significant wave height, period and direction measured by NOWPHAS were used for the estimation (shown in Table 1). Figure 8 shows the distribution of wave height H and wave direction θ. The vertical axis is the water depth h normalized by the deep water wave length L_0. No significant increase in wave height was observed due to highly oblique incidence.

Ursell number, used as a measure of non-linearity, is defined as $Ur = gHT^2/h^2$, where g

is the gravitational acceleration and T is the wave period. The variation of Ursell number is also shown in Fig. 8. The region where $Ur < 50$ the effect of non-linearity can be neglected, which is the region of $h/L_0 \geq 0.043$ ($y \geq 1100$ m in Fig. 7); therefore, non-linear effects were not significant except in the final breaking region although a typhoon was traveling and the sea condition was stormy.

The breaking point is indicated in the figure where h/L_0 is 0.021, which is close to y = 500 m. Breaker depth index (γ_b = 0.8) was used to estimate the breaking point, which is defined as $\gamma_b = H_b/d_b$, where H_b is the wave height at incipient breaking and d_b is the depth at breaking. The values of H_b and d_b were 3.83 m and 4.8 m respectively.

Fig. 8

3.2 *Time averaged image*

A time averaged image or time exposure image can be formed from consecutive series of echo images as shown in Fig. 9, which is an average of a 17-minute image sequence at 22nd hr of July 26, 2005. A close-up around the pier with the associated bottom profile is juxtaposed. Individual waves disappear in the time averaged image and an edge extending in the long-shore direction becomes visible. Several features such as the breaker zone, shoreline position, near-shore bar crest locations etc can be estimated using the averaged image [e.g. Ruessink *et al*., 2002; Takewaka, 2005]. The incidental high waves ($H_{1/3}$ = 3.69 m from NOWPHAS records) due to the typhoon would have extended the breaking point beyond the

tip of the pier which is consistent with the estimates described in section 3.1.

Fig. 9

3.3 *Cross- and long-shore time stack*

Time stacks are composite images whose one axis represents time, and the coastal extent is the other axis. The time-space images are referred as cross-shore time stack or long-shore time stack. A line of pixels extracted from consecutive images and stacked the line side-by-side to produce a time stack image. The time stacks from radar images for long-shore and cross-shore directions are useful in visualizing features such as wave run-up motion at the swash zone, wave propagation speeds etc [e.g. Stockdon and Holman, 2000].

Cross-shore time stack images were processed for four cross-shore lines as shown in Fig. 10(a). The lateral and vertical axes are the cross-shore extent in space and the time variation, respectively. Inclinations of the white oblique lines in the diagram can be read to determine the approximate speed of the shoreward progressive waves. The bottom white points correspond to the maximum run-up positions of the individual waves. Cross-shore time stacks would also illustrate variations of wave amplitude through intensity fluctuations in time at each cross-shore location; however, we made no such estimates in this study.

Figure 10(b) shows the long-shore time stack images for four different long-shore lines. The long-shore extent in space is shown on the horizontal axis and elapsed time on the vertical. The long-shore component of wave celerity can be quantified from the gradients of

the streaks in the images.

The time stack images (Fig. 10) prepared from a sequence of original radar images contain all frequency components, which require frequency separation to estimate wave propagation speed of specific wave component.

The long-shore component of local celerity is apparently constant from offshore to onshore which can be observed through the gradient of the streaks. However, the cross-shore component decrease gradually as one move towards the shore until the near-shore region is reached where the decrease becomes rapid. The uniform gradient of the long-shore time stack confirms the long-shore uniformity during this period, which can also be observed through the time averaged image.

Fig. 10

4. Wave Field Analyses

4.1 *Frequency spectrum*

Temporal variations of echo signals at several locations were analyzed with the Fast Fourier Transform (FFT). A sequence of images of 256 s (128 images) was used in the analysis and the peak frequency corresponding to the highest spectral density was determined. Spatially averaged spectra for four different cross-shore coordinates (y = 600 m, 1000 m, 1500 m and 2000 m) are shown in Fig 11(a). Each spectrum was formed by averaging over 128 pixels in the long-shore direction and was normalized between 0 and 1. The same peak frequency f_p of

0.066 Hz was observed for the different cross-shore locations.

Figure 11(b) shows the results of the FFT analyses displayed as an image. Spectra were averaged spatially and normalized in the same way as described above. The brightness of the image corresponds to higher spectral strength. The figure depicts the cross-shore uniformity of the peak frequency, 0.066 Hz (= 15.1 s). The spectral analysis gives a somewhat lower dominating frequency than the NOWPHAS record for the significant wave, 0.0826 Hz (= 12.1 s).

The peak frequencies were estimated from the radar images for different hours and compared with the NOWPHAS record for the significant wave period (Fig. 6). The estimated peak periods as well as the significant wave periods have an almost constant trend.

Fig. 11

4.2 *Wavenumber-frequency spectrum*

Wavenumber-frequency spectra were estimated with three dimensional FFT. A window of size 1389 m × 694.5 m (256 pixels × 128 pixels) and subsequent images of 256 s (128 images) were analyzed. The window size in the y-direction was reduced to half (256 pixels × 64 pixels) for spectrum analysis of the onshore region because the wave length component in the cross-shore direction decreases from offshore to onshore. Fig. 12 shows the wavenumber spectra for the peak frequency f_p (0.066 Hz) and $2f_p$ (0.137 Hz). The directional variation during wave propagation can be derived from the figure. The mean water depth of the

window area h_{mean} was estimated from the bathymetric chart and the corresponding wavenumber k_m for the peak frequency estimated with the linear theory is also shown in the figure as a dotted line.

The frequency spectrum has some energy concentration at $2f_p$, which doesn't agree with the linear dispersion relationship. These energies may have arisen due to non-linearity or saturation and truncation of the radar echo signals (shown in Fig. A-1).

Fig. 12

4.3 *Temporal filtering*

The sequence of radar images was filtered at the dominant Fourier component of the radar signals corresponding to the peak frequency f_p. Complex amplitude of the frequency component f_p at every pixel was used to generate a sequence of filtered images. Fig. 13 shows the relative phase distribution of the filtered image along with the original image. The filtered phase image reveals the prevailing wave crests with some noisy locations where returned echoes were weak. The train of wave crests is approaching obliquely towards the shore which is clearly shown in the filtered phase image. The refraction angle was quantified from this image as described in the following section.

Fig. 13

4.4 *Cross-shore distribution of wavenumber*

The filtered image sequence represents the passage of a dominant wave and was used here to

estimate the distributions of wave number components. The Fast Fourier Transform (FFT) and Maximum Entropy Method (MEM) were used for the estimation.

4.4.1 *Estimation with the Fast Fourier Transform (FFT)*

The x and y components of wave number, k_x and k_y, for the dominating wave component were estimated by applying FFT in a small window on the filtered image and considering the peak value from the averaged spectrum. The horizontal dimension of the local window was kept constant to 1389.0 m (256 pixels). The vertical dimension of the window in the offshore regions was set to 694.5 m (128 pixels) and reduced to half of that in the near shore regions. Figure 14 shows the cross-shore distribution of the wave number components and their corresponding wavelength at x = 1500 m. The wave angle defined by $\theta = \tan^{-1}(k_y/k_x)$ is the refraction angle for the dominating wave and is shown in Fig. 14.

The constant distribution of k_x could be confirmed from the almost uniform oblique streaks in the long-shore time stack shown in Fig. 10(b), whereas k_y varies in a stepwise manner and decreases towards the shore which is in accordance with the cross-shore time stack shown in Fig. 10(a). The stepwise variation is due to the limitation of the spatial resolution of the FFT analyses.

Fig. 14

4.4.2 *Estimation with the Maximum Entropy Method (MEM)*

The wave number distributions were also estimated using the Maximum Entropy Method that provides higher resolution compared to the FFT. The estimation procedure was similar to the FFT analysis. The horizontal dimension of the window was 694.5 m (128 pixels), whereas the vertical dimension was reduced from 694.5 m (128 pixels) to 173.6 m (32 pixels) in two steps. The horizontal and vertical components of wave number variation along the cross-shore line x = 1500 m are shown in Fig. 14 with wave length L and wave angle θ. The MEM estimation results in a smooth distribution of wave parameters. In the radar image shown in Fig. 13, the refraction angles are gradually increasing and becoming normal to the shore with decreasing depth from offshore to onshore, which is confirmed by both the MEM and FFT estimates.

4.5 *Wave ray computation*

The changes of wave number k and wave angle θ were computed with a ray tracing procedure [e.g. Dean and Dalrymple, 1984] to compare with the radar estimates. The bathymetric data collected from the Maritime Safety Agency, which is described in section 2.5, were used in this computation. The wave angle at offshore locations used for ray analyses was deduced from the NOWPHAS record. Numerical computation of wave ray patterns was done for waves with a 15.1 s (0.066 Hz) period which corresponds to the peak frequency of the radar signals. Fig. 15 shows the computed wave ray patterns for the coverage of the radar

measurements. The figure also shows the depth contours at every 2.0 m in depth. The wave approached obliquely, refracted slowly until it reached a water depth of 10 m (y < 1500 m), and finally refracted rapidly when it came close to the shore which can be seen from the ray patterns.

Fig. 15

The wave angles estimated from the wave ray computation and from the filtered radar image along x = 1500 m are compared in Fig. 16. Maximum deviation and standard deviation estimated from the comparison of the results are 4.13˚ and 0.813˚ respectively. The estimated wave angles from filtered radar image match well with those from wave ray computation, which confirms the applicability of the linear theory.

Fig. 16

4.6 *Inversion of water depth*

Water depths h are related to local wavenumber k and frequency f through the linear dispersion equation, $\sigma^2 = gk \tanh(kh)$, where σ is the angular frequency defined as $\sigma = 2\pi f$, g is the acceleration due to gravity and $k = \sqrt{(k_x^2 + k_y^2)}$ is the wavenumber. The depths can be derived with

$$h = \frac{1}{k}\tanh^{-1}\left(\frac{\sigma^2}{gk}\right) \quad (1)$$

The water depths estimated along the pier using Eq. (1) and compared with the survey data in Fig. 17. The distribution of wavenumber required for the depth estimation was derived from the MEM analyses for the peak frequency f_p. The overall inverted water depths match fairly

well with the surveyed depths except in some regions out of the surf zone where discrepancies up to ±1.0 m have been observed.

The ability to estimate water depths becomes very sensitive to errors as L/L_0 approaches unity and the inversion technique becomes unstable [e.g. Stockdon and Holman, 2000]. The maximum inverted depth from the filtered radar image is 17.3 m and the corresponding wave length is 186 m (with f_p = 0.066 Hz) which makes L/L_0 approximately 0.53. Hence, we regard that the inverted water depth is far from the sensitive zone.

There are several possible factors affecting the depth estimation. As the water becomes shallower towards the beach, the effect of non-linearity in wave behavior become more significant, causing higher wave celerity than the linear theory predicts and hence causing an over estimate of water depths [e.g. Bell, 1999]. The influence of currents, both tidal and wave induced, are also a potential source of variability in the water depths estimation. Such currents make the derived water depths larger if the current is in the direction of wave motion or smaller if the current is in opposition to the waves [e.g. Bell et al., 2004]. The estimated water depths in the energetic zone show very good agreement (y < 400 m) with the surveyed depths, which may be due to a coincidental canceling of probable effects from different factors.

Fig. 17

5. Concluding Remarks

X-band marine radar measurements were conducted during a typhoon event and echo images

were analyzed to estimate the linear aspects of the wave field. The study was conducted at the research pier HORS located near Hasaki, Japan. We used an X-band imaging radar to provide instantaneous distributions of wave crests and their spatial and temporal variation. Water surface variations measured at the pier were compared with the radar measurements, and a significant coherence was observed between the radar echo signals and wave gauge records. Filtered phase images were constructed at the peak frequency corresponding to the dominating wave, which exhibit the refraction pattern in the near-shore region. Wave number components from the filtered phase images were estimated using the FFT and MEM. An acceptable agreement is obtained between the estimated refraction angle from the filtered phase images and the linear estimates from wave ray analyses. The water depths were estimated using linear dispersion relationship and compared with the surveyed depths giving a fairly good match except for some regions where discrepancies up to ±1.0 m were observed.

The approach described here would seem to provide a useful way for estimating the hydrodynamic parameters in a region in which it is difficult to maintain in situ measurements. While not of comparable accuracy to conventional techniques, the radar remote sensing method is logistically simple, inexpensive and robust under severe weather condition, thus the system prove to be a powerful tool for continuous monitoring of the near-shore wave field.

Acknowledgements

The authors are grateful to the members of the Littoral Drift Division, PARI, who provided assistance in radar and wave measurements and results of the depth surveys. Part of this study was financially supported by the Grants-in-Aid of the Japan Society for the Promotion of Science (JSPS).

References

Aarninkhof, S. G. J., Ruessink, B. G. & Roelvink, J. A. [2005] "Nearshore subtidal bathymetry from time exposure video images," *Journal of Geophysical Research* **110** (C06011).

Bell, P. S. [1999] "Shallow water bathymetry derived from an analysis of X-band marine radar images of waves," *Coastal Engineering* **37**, 513-527.

Bell, P. S. [2001] "Determination of bathymetry using marine radar images of waves," *Proc. Of the 4th International Symposium on Ocean Wave measurement and Analysis*, San Francisco, California, Vol. 1, pp. 251-257.

Bell, P. S., Williams, J. J., Clark, S., Morris, B. D. & Vila-Concejo, A. [2004] "Nested radar systems for remote coastal observations," *Journal of Coastal Research* **39** (SI).

Dankert, H. & Rosenthal, W. [2004] "Ocean surface determination from X-band radar image sequences," *Journal of Geophysical Research* **109** (C04016).

Dean, R. G. & Dalrymple, R. A. [1984] "Water wave mechanics for engineers and scientists," *Advanced Series on Ocean Engineering* 2, World Scientific, Singapore, p353.

Enchevort, I. M. J. V. & Ruessink, B. G. [2001] "Effect of hydrodynamics and bathymetry on video estimates of near-shore sand bar position," *Journal of Geophysical Research* **106**(C8), 16969-16979.

Holland, K. T. & Holman, R. A. [1999] "Wave number frequency structure of infragravity swash motions," *Journal of Geophysical Research* **106**(C3), 13479-13488.

Holland, K. T., Raubenheimer B., Guza, R. T. & Holman, R. A. [1995] "Runup kinematics on a natural beach," *Journal of Geophysical Research* **100**(C3), 4985-4993.

Izquierdo, P., Borge, J. C. N., Soares, C. G., Gonzalez, R. S. & Rodriguez, G. R. [2005] "Comparison of wave spectra from nautical radar images and scalar buoy data," *J. of Waterway, Port, Coastal and Ocean Eng., ASCE* **131**(3), 123-131.

Lippman, T. C. & Hollman, R. A. [1989] "Quantification of sand bar morphology: A video technique based on wave dissipation," *Journal of Geophysical Research* **94**(C1), 995-1101.

Plant, N. G. & Holman, R. A. [1997] "Intertidal beach profile estimation using video images," *Marine Geology* **140**, 1-24.

Piotrowski, C. C. & Dugan, J. P. [2002] "Accuracy of bathymetry and current retrievals from airborne optical time series imaging of shoaling waves," *IEEE Transactions on*

Geoscience and Remote Sensing **40**(12), 2606-2618.

Ranasinghe, R., Symonds, G., Black, K. & Holman, R. [2004] "Morphodynamics of intermediate beaches: a video imaging and numerical modeling study," *Coastal Engineering* **51**, 629-655.

Ruessink, B. G., Bell, P. S., Van Enckevort, I. M. J. & Aarninkhof, S. G. J. [2002] "Nearshore bar crest location quantified from time-averaged X-band radar images," *Coastal Engineering* **45**, 19-32.

Stockdon, H. F. & Holman, R. A. [2000] "Estimation of wave phase speed and nearshore bathymetry from video imagery," *Journal of Geophysical Research* **105**(C9), 22015-22033.

Takewaka, S. [2005] "Measurements of shoreline positions and intertidal foreshore slopes with X-band marine radar system," *Coastal Engineering Journal*, *JSCE* **47**, 91-107.

Takewaka, S. & Nishimura, H. [2005] "Wave run-up analyses during a storm event with nautical X-band radar," *Proc. of Asian and Pacific Coasts on CD-Rom* (*APAC* 2005), Korea.

Young, I. R., Rosenthal, W. & Ziemer, F. [1985] "A three-dimensional analysis of marine radar images for the determination of ocean wave directionality and surface currents," *Journal of Geophysical Research* **90**(C1), 1049-1059.

Appendix Correlation between Radar Echoes and Water Surface Elevations

Coherence between radar echoes and wave gauge records was estimated to examine the utility of radar backscatter. The radar images are updated every 2.0 s and water surface elevations at several locations along the pier are recorded every 0.5 s; however, the measured wave data during the typhoon BANYAN (T7) was noisy. Hence, the comparison was done using records for another storm, which passed near HORS in 2002 (Typhoon #6, T6, 2002: Typhoon CHATAAN) because the radar image sequences for this typhoon clearly revealed oblique waves approaching the shore similar to those generated by T7 in 2005. The horizontal and vertical extent of the images were one-third during typhoon CHATAAN observation compared to the images of T7, so the corresponding pixel dimension reduced to a square of 1.8 m.

Variation of the pixel intensity at a point x = 9 m, y = 230 m from an image sequence of 256 images (about 8.5 minutes) were compared with the water surface elevations measured by a wave gauge located at x = 0 m, y = 230 m as shown in Fig. A-1. Frequent signal saturations are observed in the radar signal time series. The horizontal shift for the radar pixel extraction is to avoid signal saturation due to existence of pier.

Fig. A-1

The rotation period of the antenna is not rigidly fixed and is affected by the wind field, leading to some fluctuations. The image sequence has a non-updated sweep since the imaging intervals (2.0 s) are shorter than the rotational time of the antenna (~ 2.5 s). This may produce

high frequency noise in the Fourier analyses.

The averaged and normalized spectra of the radar pixel intensity and water surface records are shown in Fig. A-2. The spectra of the radar data were formed through spatial averaging, whereas the wave gauge records through temporal averaging. The spectra have a similar shape with frequency peaks positioned close to same peak frequency (~ 0.115 Hz) and spectral energy distributions within 0.035 ~ 0.25 Hz.

Fig. A-2

The coherence and phase of the recorded signals are shown in Fig. A-3. The figure depicts a relatively high coherence for the frequency band 0.06 to 0.17 Hz. The phase lag between the radar signals and water surface elevations gradually increased up to 90˚ (≈ 1.0 *s*) at the frequency of 0.25 Hz. Since the radar echoes were sampled 9 m (5 pixels) away from the wave gauge location, the wave crests took this time to travel this distance.

Figure A-3 also shows radar signal and water surface variation after being filtered through a band pass filter (0.06 Hz to 0.17 Hz) and normalized by the difference of the maximum and minimum values. The figure shows that the filtered echo signals follow reasonably well with the passage of wave crests which means the phases are correlated. It is however, hard to find a systematic relationship between the wave height of individual waves and the echo signal intensity by just applying a band pass filter.

Fig. A-3

Table 1: NOWPHAS wave records for 22nd hr of July 26, 2005

Significant wave height $H_{1/3}$	3.69 m
Significant wave period $T_{1/3}$	12.1 s
Significant wave direction $\theta_{1/3}$	33°

Table 2: Period of the bathymetric surveys around HORS and their area coverage

Period of the survey	Long-shore coverage [m]	Cross-shore coverage [m]	Note
On weekdays	$x = 0$	y < 385	Survey along the pier
2000, 2001, 2002, 2005	- 300 < x < 300	- 110 < y < 930	Survey around HORS with back-shore coverage
1989	- 1000 < x < 1000	- 110 < y < 4490	Extended survey around HORS with back-shore coverage
Data collected until 1977	Full coverage of the area of interest		Surveyed by the Maritime Safety Agency (map # 6367-7), issued 1977

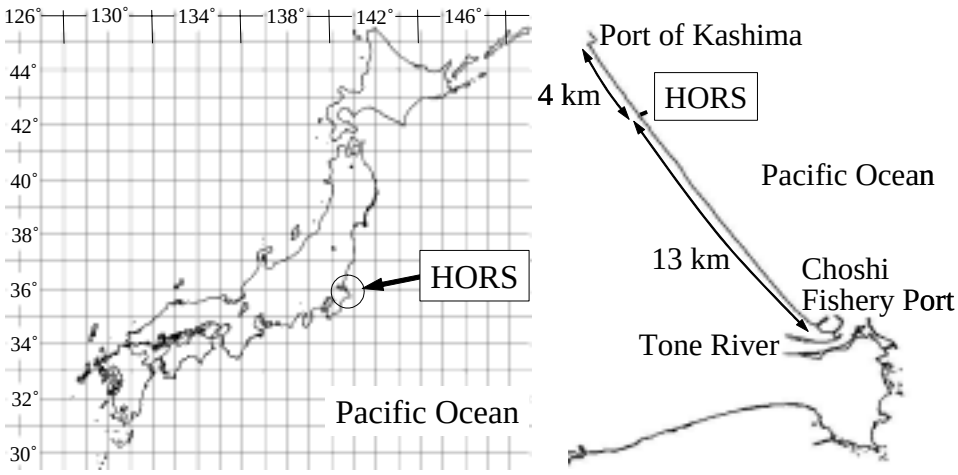

Fig. 1: Location of Hasaki Oceanographical Research Station (HORS).

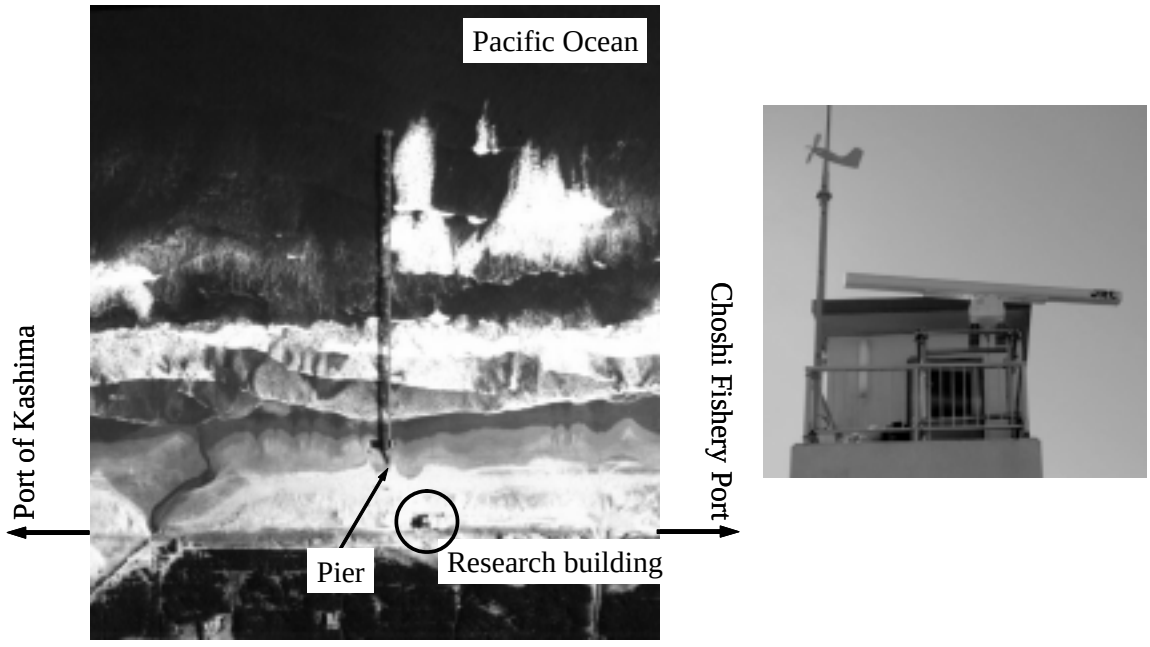

Fig. 2: Aerial view of the Hasaki observation pier (left photo) and radar antenna (length ~ 2.8 m) on the roof of the research building (right photo).

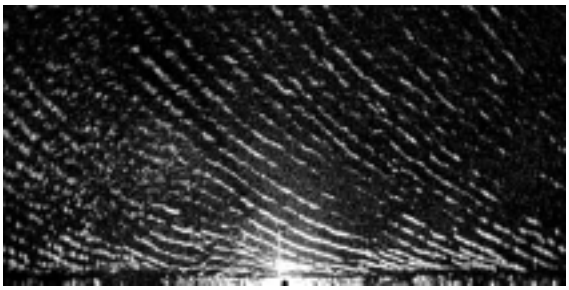

(a)

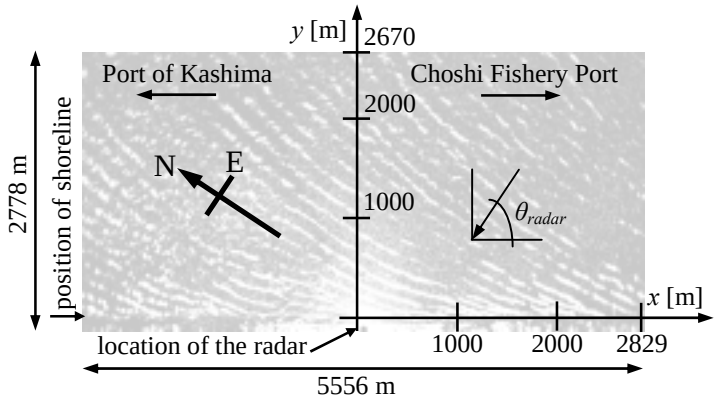

(b)

Fig. 3: (a) Radar echo image and (b) the coordinate system.

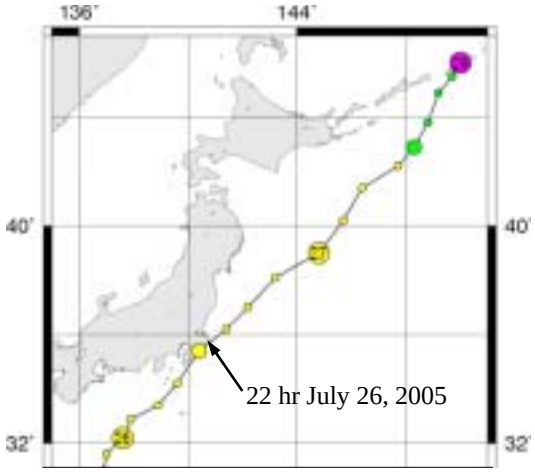

Fig. 4: Path of the typhoon BANYAN (T7), July 21 ~ 31, 2005.
(http://agora.ex.nii.ac.jp/digital-typhoon).

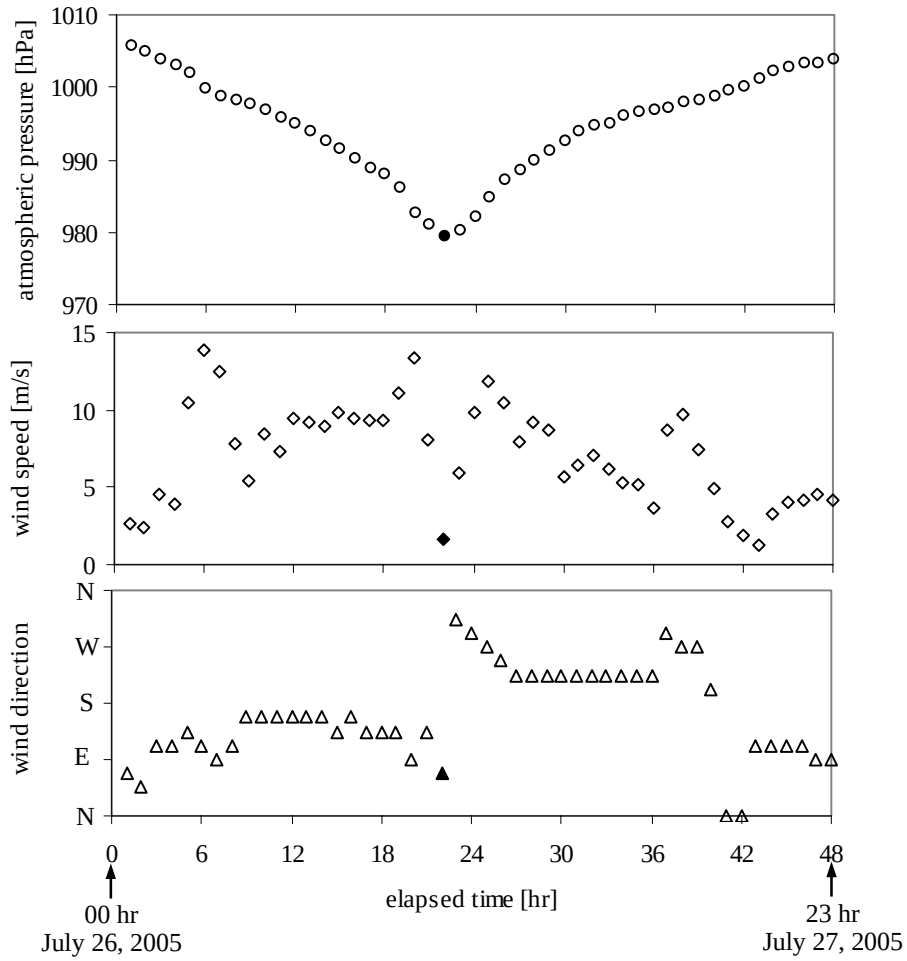

Fig. 5: Atmospheric pressure, wind speed and wind direction observed at Choshi Fishery Port during the storm T7. Detailed analyses were conducted for the period depicted with solid symbols.

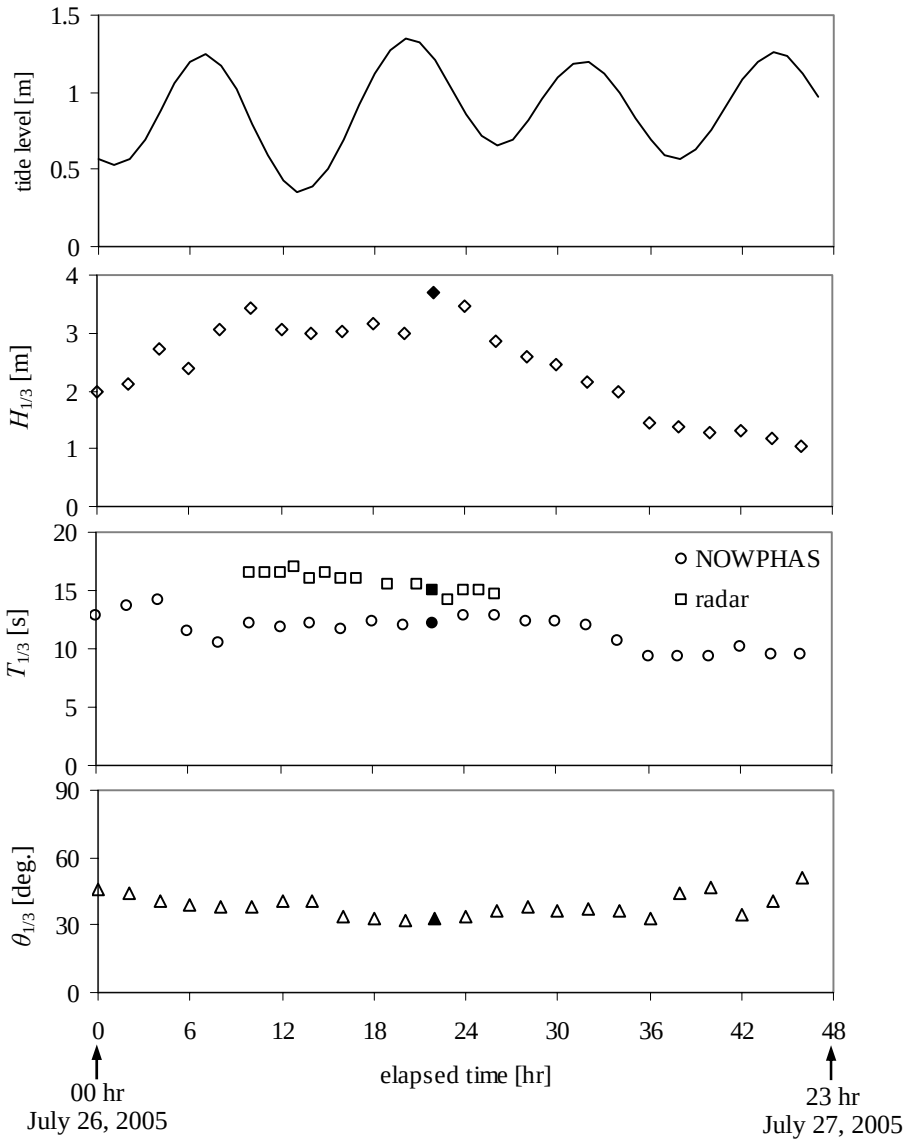

Fig. 6: Tide level measured at Choshi Fishery Port by the Japan Meteorological Agency and significant wave height $H_{1/3}$, significant wave period $T_{1/3}$ and significant wave direction $\theta_{1/3}$ measured at Kashima Port. Average peak period estimated from available radar data during typhoon T7 also compared with $T_{1/3}$. Solid symbols indicate the analyzing period. (NOWPHAS, http://infosv2.pari.go.jp/bsh/ky-skb/kaisho/eng/marine_home_e.htm)

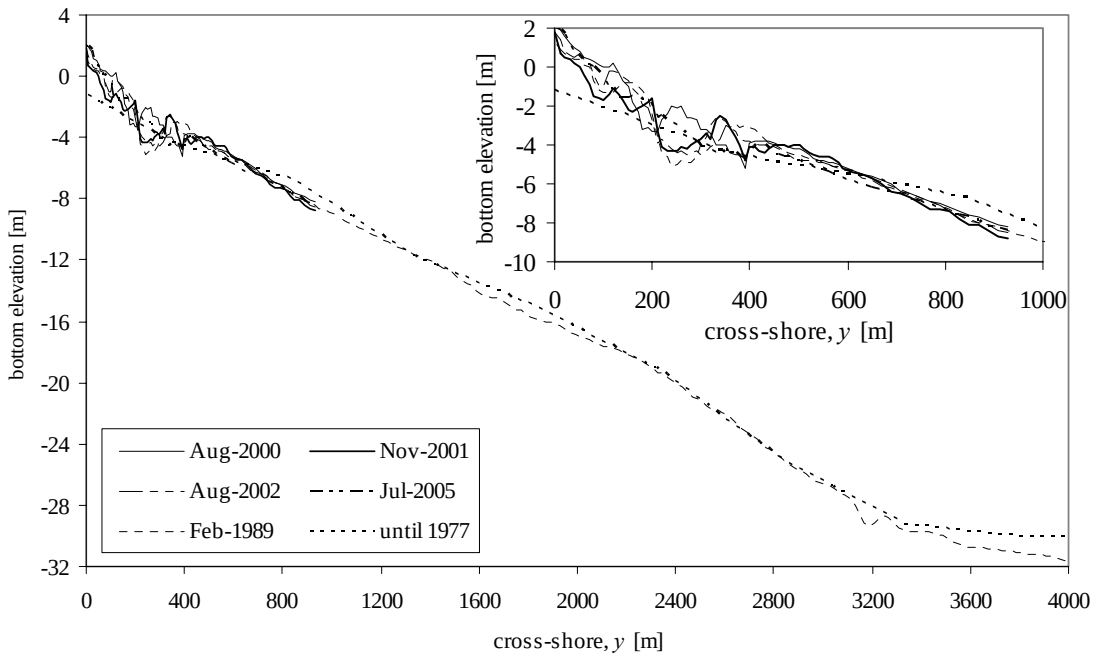

Fig. 7: Surveyed bottom elevations along the pier (x = 0 m).

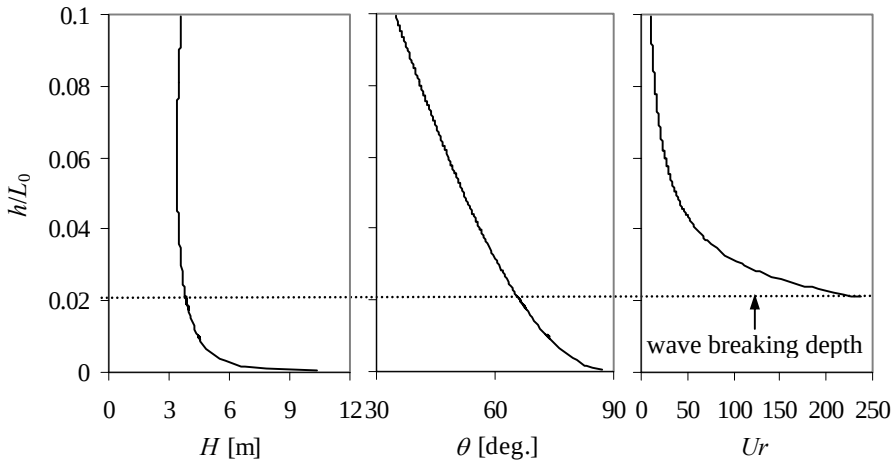

Fig. 8: Distribution of wave height H, wave direction θ and Ursell number Ur estimated with linear theory. The offshore values were collected from NOWPHAS records ($H_{1/3}$ = 3.69 m, $T_{1/3}$ = 12.1 s, $\theta_{1/3}$ = 33˚ at 24 m water depth).

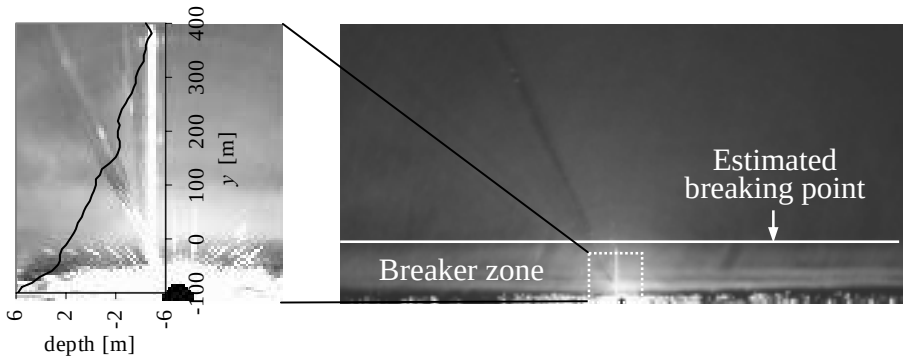

Fig. 9: Averaged radar image for 22nd hr of July 26, 2005.

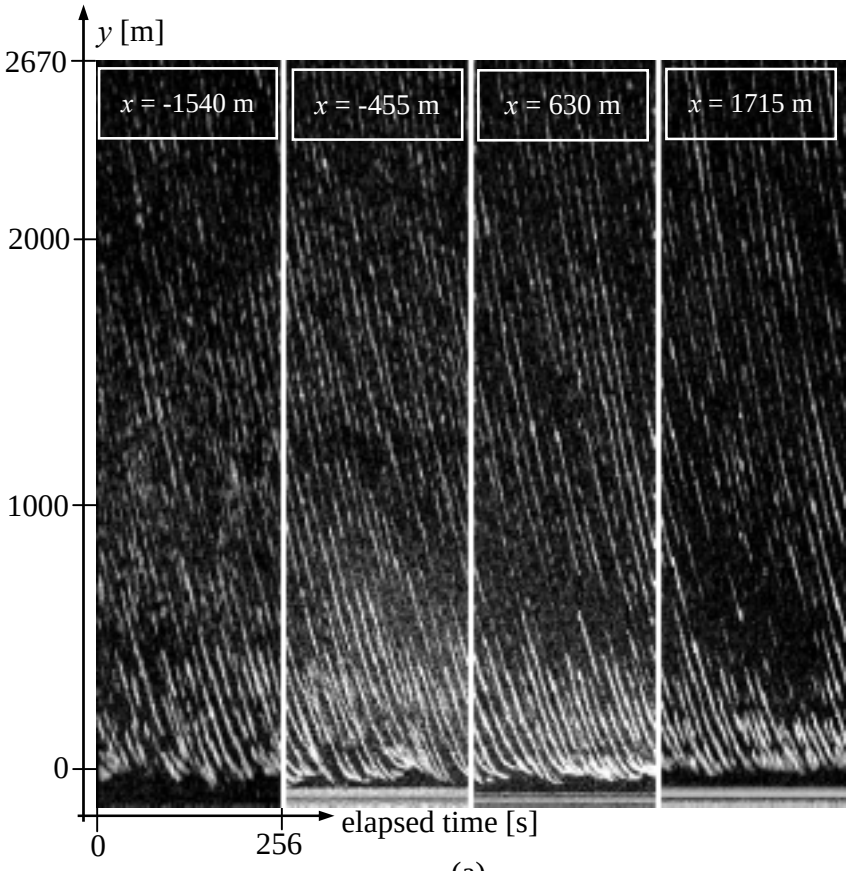

(a)

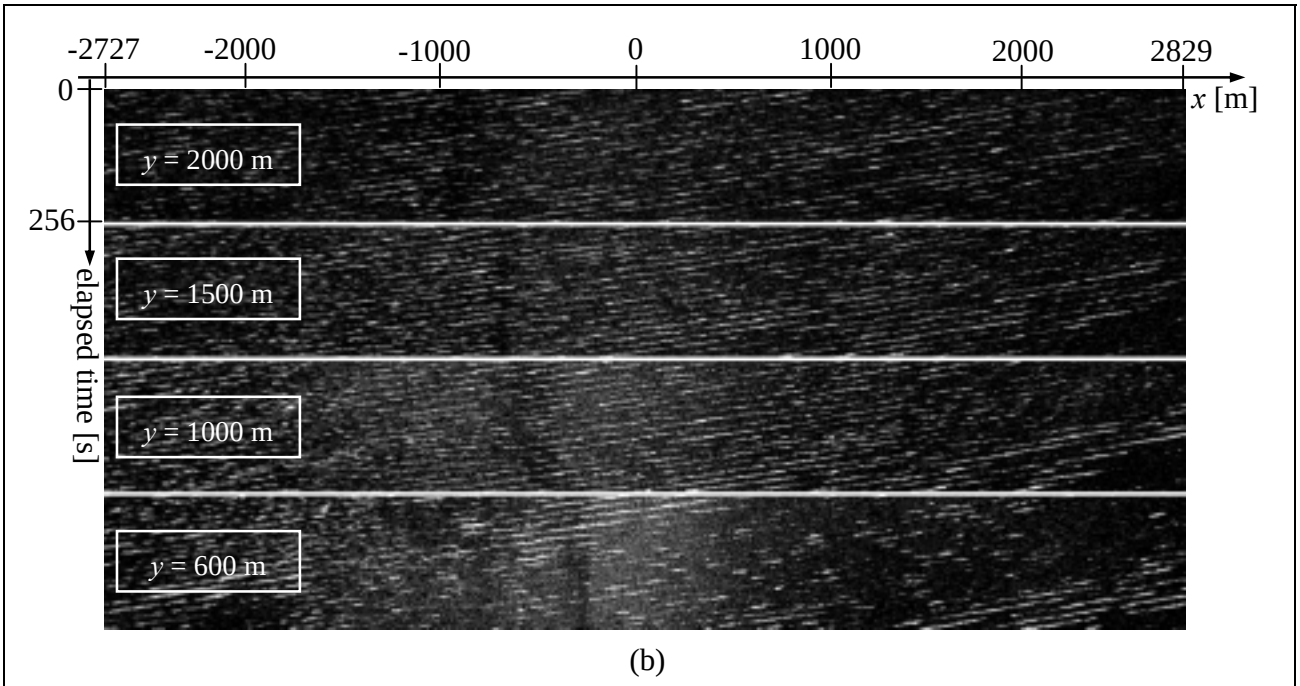

Fig. 10: (a) Cross-shore and (b) long-shore time stacks at different locations for 22nd hr of July 26, 2005.

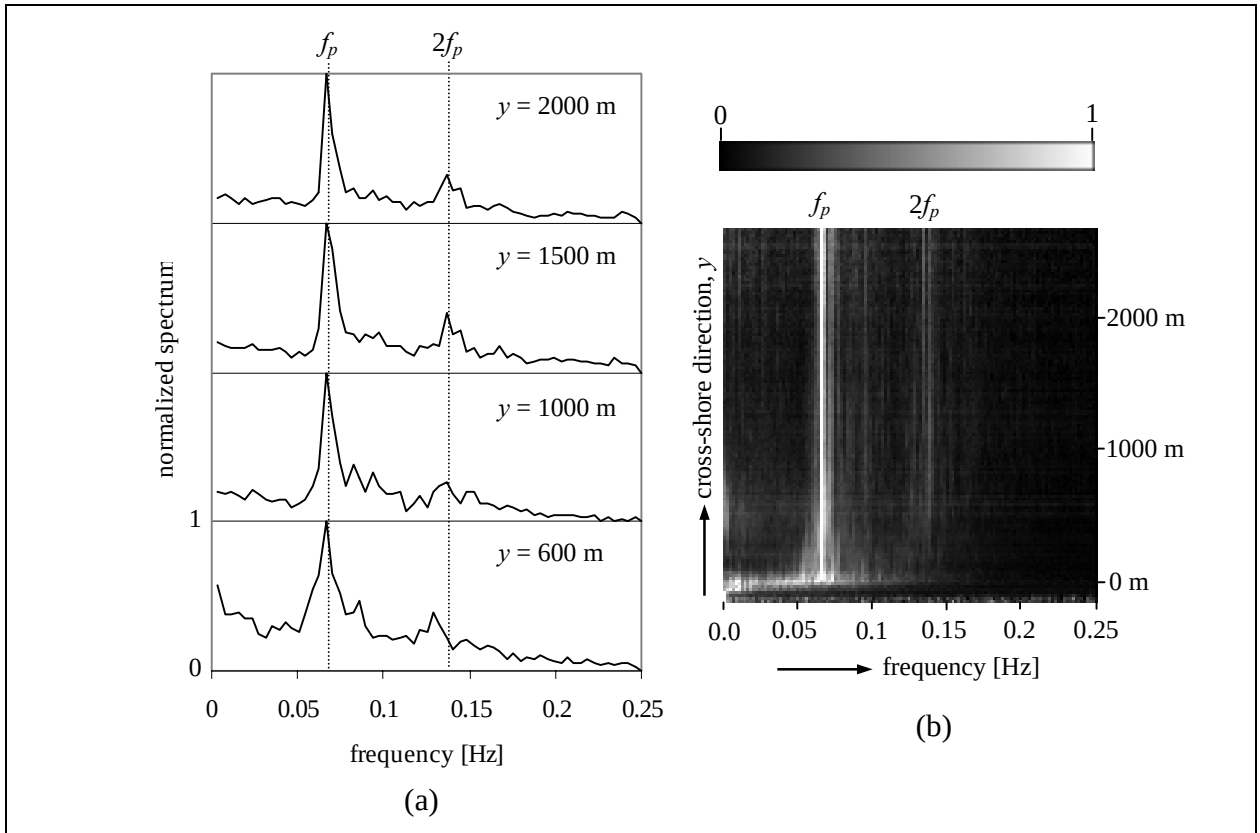

Fig. 11: Averaged and normalized cross-shore spectra at x = 2135 m for 22nd hr of July 26, 2005.

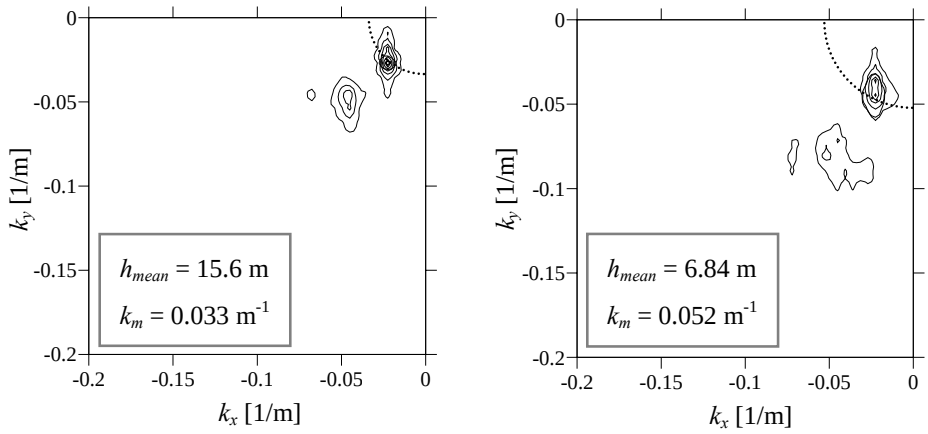

Fig. 12: Wave number spectra for f_p (peak frequency = 0.066 Hz) and $2f_p$ at (a) offshore (x = 1500 m, y = 2000 m) and (b) onshore (x = 1500 m, y = 600 m) locations. Dotted line represents the mean wave number k_m corresponding to the mean water depth h_{mean} of the local region.

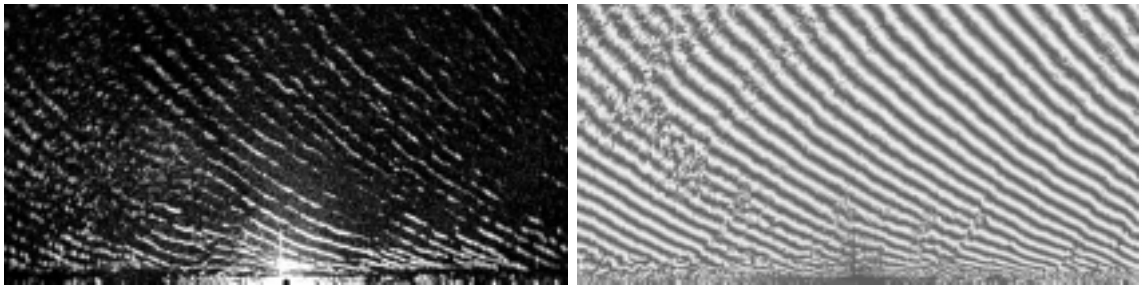

Fig. 13: (a) Original radar image (22 hr July 26, 2005) and (b) filtered (with f_p) phase image.

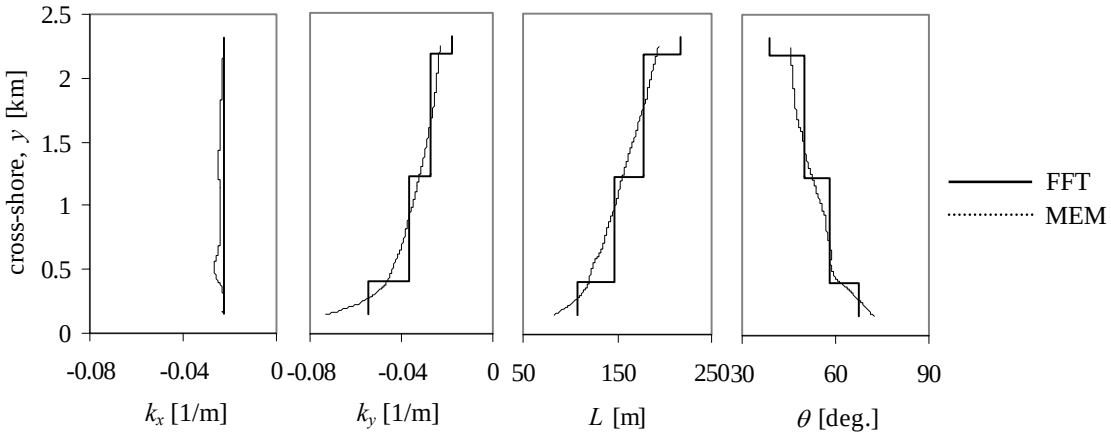

Fig. 14: Cross-shore distribution of wave number components with wave length and wave angle along x = 1500 m estimated from a filtered image.

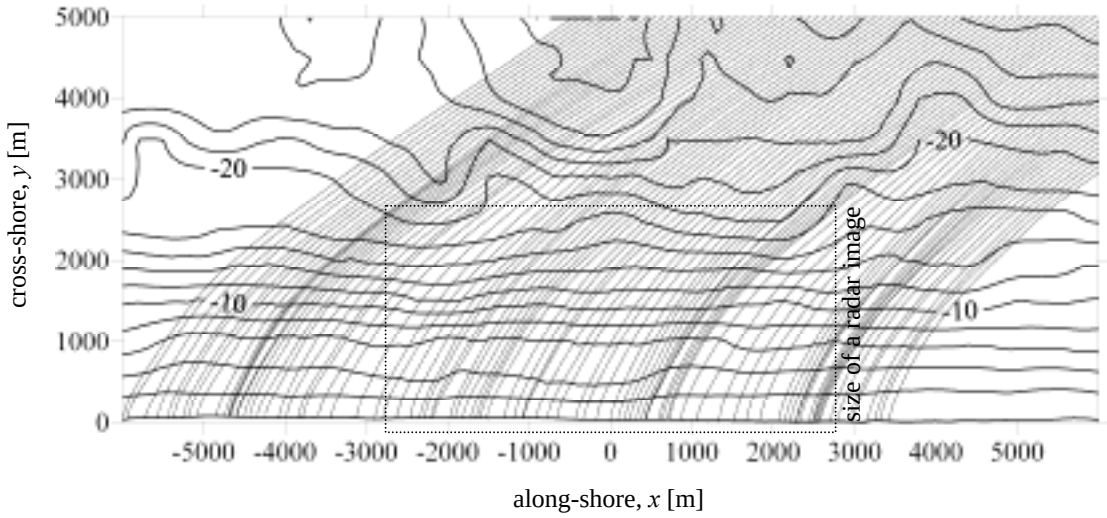

Fig. 15: Wave ray patterns and bathymetric contours at every 2.0 m water depth. The dotted box shows the extent of a radar image.

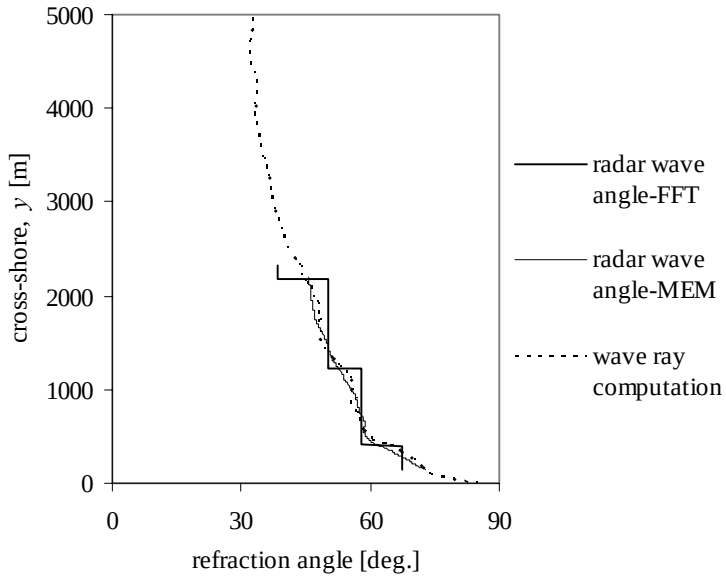

Fig. 16: Comparison between refraction angles estimated from radar image and wave ray analyses. Refraction angle 90˚ corresponds to shore normal incidence.

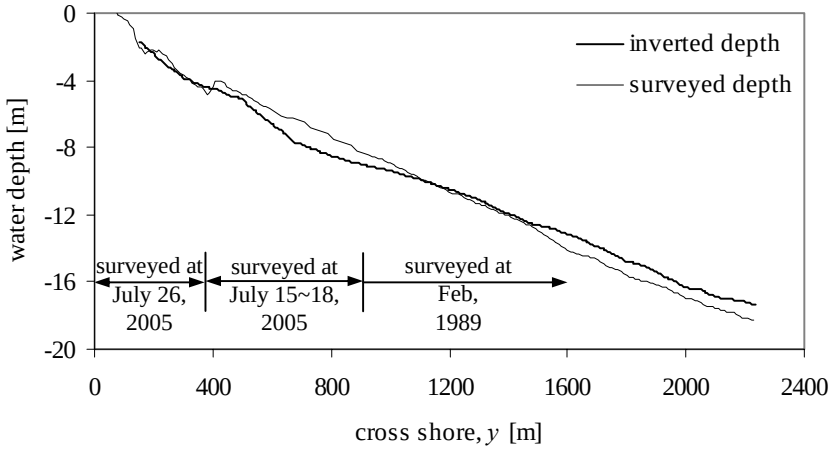

Fig. 17: Comparison between inverted water depths estimated from radar image and surveyed data along the pier (x = 0 m).

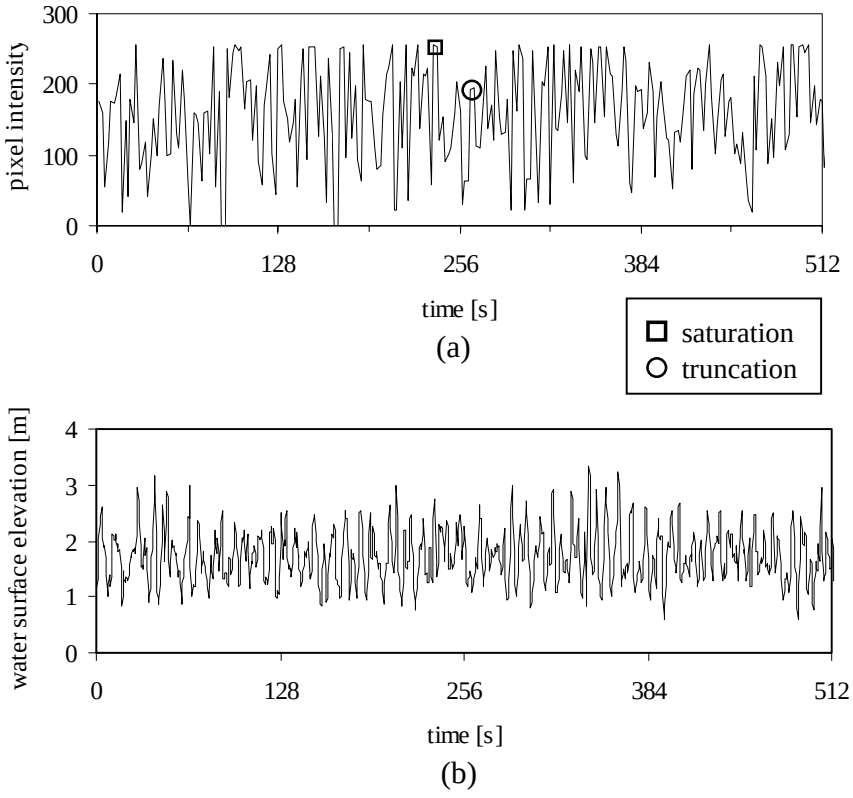

Fig. A-1: Variation of (a) radar echo intensity (sampling frequency 0.5 Hz) and (b) water surface elevation (sampling frequency 2.0 Hz) at (x = 0, y = 230 m) measured during typhoon CHATTAN (T6, 2nd hr of July 11, 2002). Open symbols on the upper panel indicate locations of a saturation and a truncation of the radar echo as examples.

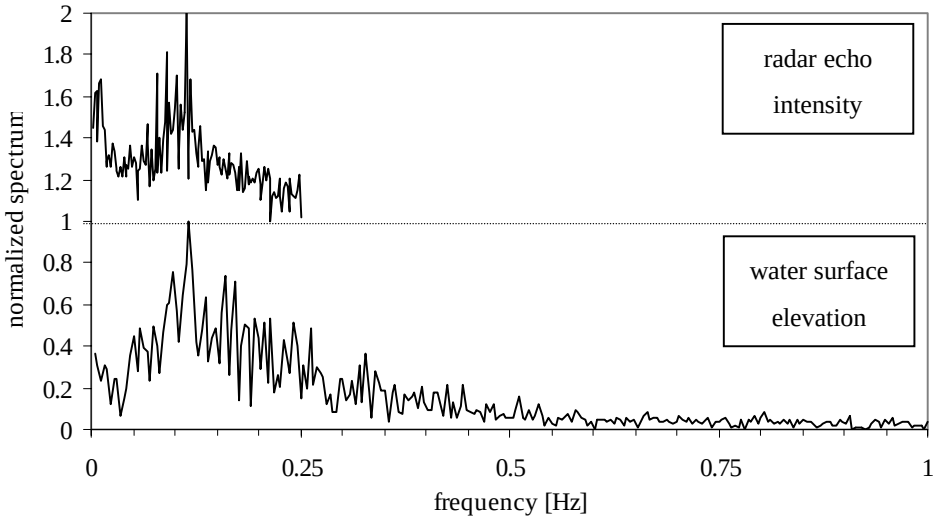

Fig. A-2: Averaged and normalized spectra of radar echo signals and water surface elevations.

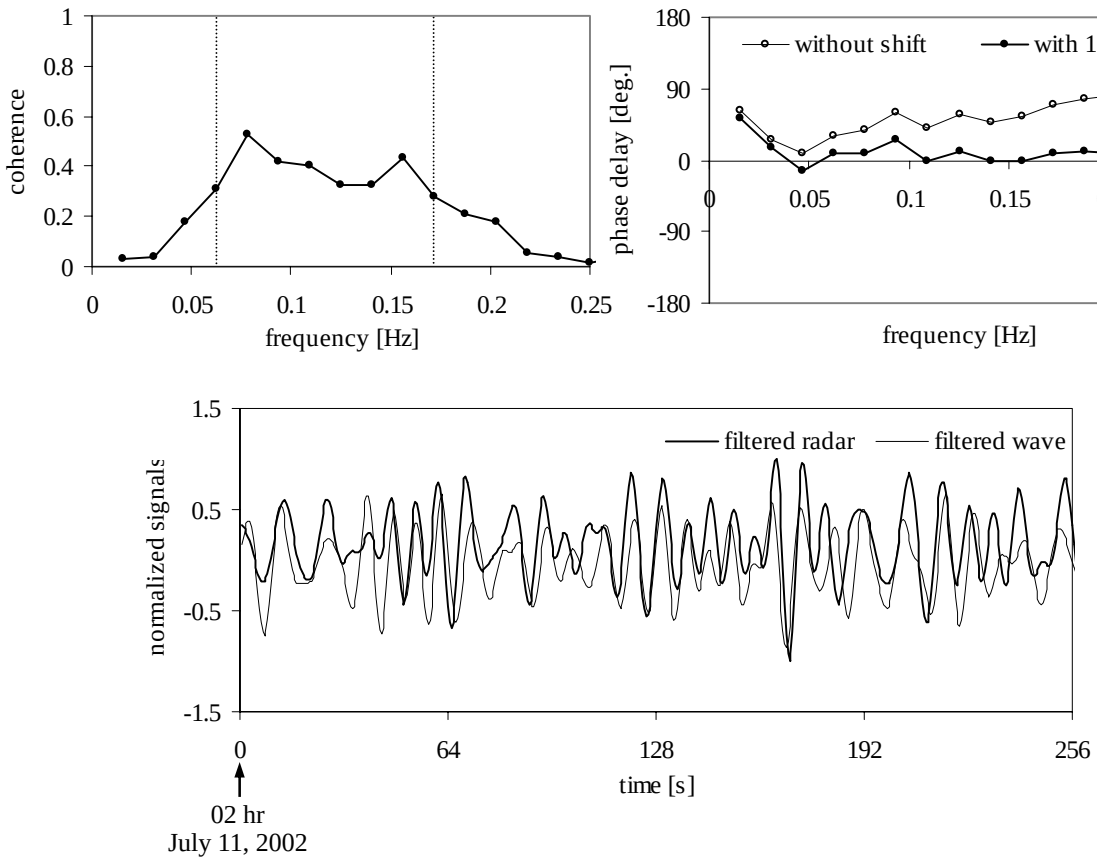

Fig. A-3: Coherence and phase delay between the time series of radar echo signals and water surface elevations (upper panel). The phase was estimated with original time series and also with shifting the water surface elevations time series by 1.0 s. Band pass filtered (0.06-0.17 Hz) radar echo signals and water surface elevations (lower panel).